Article

Comparative Study of High-resolution LysB29(Nε-myristoyl) des(B30) Insulin Structures Display Novel Dynamic Causal Interrelations in Monomeric-Dimeric Motions

Esra Ayan[1], Ebru Destan[1], Abdullah Kepceoglu[1], Halil Ibrahim Ciftci[1] , Ahmet Katı[2] and Hasan DeMirci[1,3,4,*]

[1] Department of Molecular Biology and Genetics, Faculty of Science, Koç University, Istanbul, Türkiye
[2] Department of Basic Medical Sciences, Division of Medical Biology, Faculty of Medicine, University of Health Science, Istanbul, Türkiye
[3] Koç University Isbank Center for Infectious Diseases (KUISCID), Koç University, Istanbul, Türkiye
[4] Stanford PULSE Institute, SLAC National Laboratory, Menlo Park, CA, USA
* Correspondence: hdemirci@ku.edu.tr, hdemirci@stanford.edu

Abstract: The treatment of insulin-dependent diabetes mellitus is characterized by artificial supplementation of pancreatic β-cell ability to regulate sugar levels in the blood. Even though various insulin analogs are crucial for reasonable glycemic control, understanding the dynamic mechanism of the insulin analogs may help to improve the best-protracted insulin analog to assist people with Type 1 Diabetes (T1D) to live comfortably while maintaining tight glycemic control. Here we present the high-resolution crystal structure of NN304, known as insulin detemir, to 1.7 A resolution at cryogenic temperature. We computationally further investigated our crystal structure's monomeric-dimeric conformation and dynamic profile by comparing it with a previously available detemir structure (PDB ID: 1XDA). Our structure (PDB ID: 8HGZ) obtained at elevated pH provides a distinct alternative dimeric conformation compared to the previous structure, suggesting it might induce an intermediate state in the dissociation pathway of the insulin detemir's hexamer:dihexamer equilibrium. Combined with orientational cross-correlation analysis by Gaussian Network Model (GNM), this alternate oligomeric conformation offers the distinct cooperative motions of a protracted insulin analog that has not been previously observed.

Keywords: long-acting insulin; detemir; X-ray crystallography; insulin dynamics; Gaussian Network Analysis

1. Introduction

In recent years the number of individuals with diabetes has increased at a higher rate in low and middle-income countries than in high-income countries (WHO). Additionally, in 2019, diabetes was recorded as the ninth leading cause of death, considering a predicted 1.5 million deaths directly caused by diabetes (WHO). Pancreatic insulin delivery can be challenging to reproduce by subcutaneous injection [1]. Among individuals with both Type 1 Diabetes (T1D) and Type 2 Diabetes (T2D), the majority of the patients fail to manage glycemic targets resulting in an increased risk of various complications [2]. The primary purpose of insulin therapy relies on the formulation of both long-acting and rapid-acting insulin analogs. Insulin therapy mimics the function of physiological insulin secretion levels to control endogenous hepatic glucose levels in the blood [3]. Recombinant insulin is a critical peptide hormone for treating insulin-dependent diabetes mellitus (DM) [3,4]. During the last decade, insulin preparations have been significantly modified to reduce the risk of health complications due to breakthroughs in the understanding of insulin structure and its complex aggregation properties [5]. The efficiency, efficacy and simplicity of insulin analogs can facilitate the patient's transition to insulin therapy [6]. Moreover, studies have revealed insulin therapy's benefits, including the use of insulin analogs that offer various advantages over human insulin [6,7]

 doi:10.20944/preprints202211.0412.v1

(Figure S1). Various insulin analogs provide advantages consisting of greater convenience (Figure S1), improved physiologic profile and a reduced risk of hypoglycemia [8]. It is of considerable importance that insulin analogs are long-acting, predictable, and have a flat pharmacodynamic profile to limit the risk of hypoglycemia in diabetic patients [8].

The active form of insulin circulates in the blood as a monomer protein consisting of two polypeptide chains: an A chain of 21 amino acids and a B chain of 30 amino acids. Insulin is produced by pancreatic β-cells as a monomer and stored in a hexameric form. The hexameric form is generated by three insulin dimers aggregating around two central zinc cations [7]. Various insulin analogs exist in the market which have been genetically engineered and formulations characterized by residual substitutions over the recombinant DNA technology [9]. Over the years, the commonly known strategy to produce a long-acting insulin variant is to formulate amorphous suspensions or crystalline insulin that provide a slowly dissolvable depot by subcutaneous injection [10].

The LysB29-tetradecanoyl, des-(B30) human insulin (NN304, insulin detemir) was introduced to the market with the brand name Levemir® in the mid-late 90s [11]. Detemir has been created as a neutral, soluble insulin preparation by covalently linking a hydrophobic myristate fatty acid chain to Lys 29 in chain B which is not strictly essential for the activity of human insulin [11]. The unique mechanism of this covalently modified insulin analog relies on its reversible binding to human albumin through the fatty acid extension [6,11]. This albumin bound form of insulin serves as a reservoir that continually and slowly releases detemir insulin into the bloodstream and delays the hormone's action [6,11,12] (Figure S2). Detemir has demonstrated greater efficacy and reproducible absorption rate compared to neutral protamine hagedorn (NPH) insulin and insulin glargine [13,14,15]. This is why detemir has had a favorable profile in clinical usage for over a decade.

Collection of studies have been conducted on detemir to understand its structure, function, and its interaction with serum albumin [12,16]. In this work, we present the high-resolution detemir crystal structure determined to 1.7 Å resolution at the cryogenic temperature. Diffraction data collected at the Turkish Light Source (AKA *Turkish DeLight*) [17]. Additionally, we employed computational Gaussian Network Model (GNM) analysis that we aimed at investigating the differences of monomer:dimer equilibrium dynamics between our high-resolution cryogenic structure with previously published detemir structure (PDB ID: 1XDA). The crystallographic data presented here provide a distinct novel unit cell origin compared to the previously published detemir unit cell orientation [11]. GNM analysis performed on the high-resolution structure also displays a previously unobserved pattern of monomeric-dimeric correlated motion of this long-acting insulin analog. Understanding monomer-dimer correlated motion of the detemir structure still remains to have immense importance in revealing the structural dynamics of the detemir and pharmacokinetics of this important hormone. This will pave the way for improving, modulating, and optimizing the protracted dissociation rate of the hexameric form of detemir into its active monomeric form

2. Results

Throughout the analysis of the manuscript, the renumbered version of 8HGZ and 1XDA structures were used and uploaded as a supplementary file (File S1) under the name Renumbered_8HGZ.pdb , and Renumbered_1XDA.pdb , respectively

2.1. Crystal Structure of Novel Detemir Crystal Form

The cryogenic detemir structure determined to 1.7 Å resolution contains four nearly identical monomer molecules in the asymmetric unit cell, as well as four myristic acid side chains, four phenol molecules, four zinc ions, four chloride ions, and 188 water molecules (Figure 1; Figure S3; FigureS 4; Table 1).

Preprints (www.preprints.org) | NOT PEER-REVIEWED | Posted: 22 November 2022 doi:10.20944/preprints202211.0412.v1

Table 1. Data collection and refinement statistics.

Dataset	Insulin detemir
PDB ID	8HGZ
Data collection	
Beamline	Turkish Light Source
Wavelength	1.5
Resolution range	21.64 - 1.7 (1.761 - 1.7)
Space group	R 3 :H
Unit cell	78.885 78.885 79.272 90 90 120
Total reflections	110176 (9012)
Unique reflections	20225 (1834)
Multiplicity	5.4 (4.5)
Completeness (%)	96.94 (90.88)
$I / \sigma I$	23.33 (3.28)
Wilson B-factor	16.70
R_{merge}	0.05 (0.39)
R_{meas}	0.05 (0.44)
R_{pim}	0.02 (0.20)
CC1/2	0.99 (0.87)
*CC**	1 (0.96)
Refinement	
Reflections used in refinement	19616 (1834)
Reflections used for R-free	1939 (179)
R-work	0.21 (0.26)
R-free	0.24 (0.28)
CC(work)	0.95 (0.81)
CC(free)	0.93 (0.76)
macromolecules	1601
ligands	103
solvent	188
Protein residues	200
RMS(bonds)	0.00
RMS(angles)	0.52
Ramachandran favored (%)	100.00
Ramachandran allowed (%)	0.00
Ramachandran outliers (%)	0.00
Rotamer outliers (%)	0.55
Average B-factor	25.64
macromolecules	24.09
ligands	34.46
solvent	34.07

Statistics for the highest-resolution shell are shown in parentheses

Preprints (www.preprints.org) | NOT PEER-REVIEWED | Posted: 22 November 2022 doi:10.20944/preprints202211.0412.v1

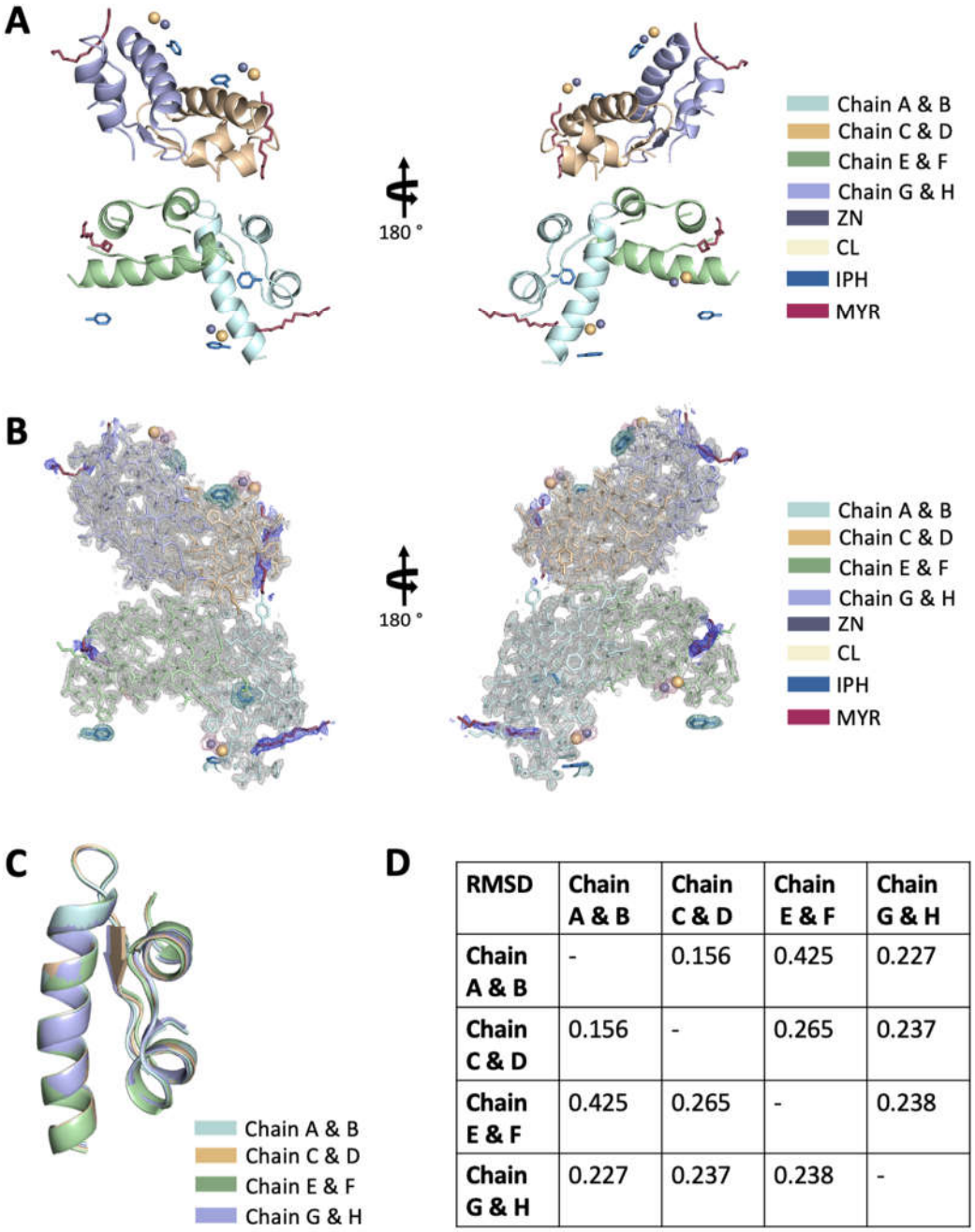

RMSD	Chain A & B	Chain C & D	Chain E & F	Chain G & H
Chain A & B	-	0.156	0.425	0.227
Chain C & D	0.156	-	0.265	0.237
Chain E & F	0.425	0.265	-	0.238
Chain G & H	0.227	0.237	0.238	-

Figure 1. The 8HGZ structure at cryogenic temperature. (A) Detemir structure is represented in cartoon view. Myristic acid (MYR), zinc (ZN), chloride (CL), and phenol (IPH) are shown in stick representation. (B) The refined 2Fo-Fc electron density map covering detemir is shown in gray, electron density for MYR is colored in blue, ZN and CL are colored in dark salmon, and IPH is colored in smudge. (C) Each monomer of detemir is superposed in *PyMOL*, and (D) RMSD values are indicated in the table.

Our crystal structures which contain two dimers at cryogenic temperature could not be superimposed with the 1XDA structure due to the distinct crystal packing of the detemir in the asymmetric unit cells (Figure 2; Figure S5; Figure S6). A significant conformational change was observed in the orientation of the two dimers (Figure S6A). The two dimers of the 1XDA structure form introverted monomers packed side by side, while the 8HGZ structure displays each dimer forms as extroverted monomers in the asymmetric unit cell. Each disulfide bonded monomer chains are labeled as A & B, C & D, E & F, and G & H (Figure 1A, B; Figure S3A). Each extroverted monomer in dimer displays more plasticity/flexibility compared to the body/center of the four-monomer structure in the ellipsoid representation (Figure S3B). The 8HGZ structure also displays

Preprints (www.preprints.org) | NOT PEER-REVIEWED | Posted: 22 November 2022 doi:10.20944/preprints202211.0412.v1

more negative charge distribution in the structure's central region compared to its periphery (Figure S3C). While the two crystallographically independent dimers are remarkably similar in the 1XDA structure (Figure S6B, top), the first dimer of the 8HGZ structure could not be superimposed over the second dimer of 8HGZ (Figure S6B, bottom) since the first dimer of 8HGZ structure is an entirely distinct orientation when compared to all 1XDA dimers (Figure S6C). However, the second dimer of 8HGZ structure is quite similar to 1XDA's dimers position (SFigure 6D). Still, all monomers are perfectly matched by the Root Mean Square Difference (RMSD) of the main-chain atoms up to 0.35 Å (Figure 1C). Each monomer includes a 14-carbon fatty acid chain covalently conjugated to the B29 Lys residue. The myristic acids engage in the crystal contacts among the neighboring dimers, radiating out the aliphatic side chains from the crystallographic axis toward the periphery (Figure S4).

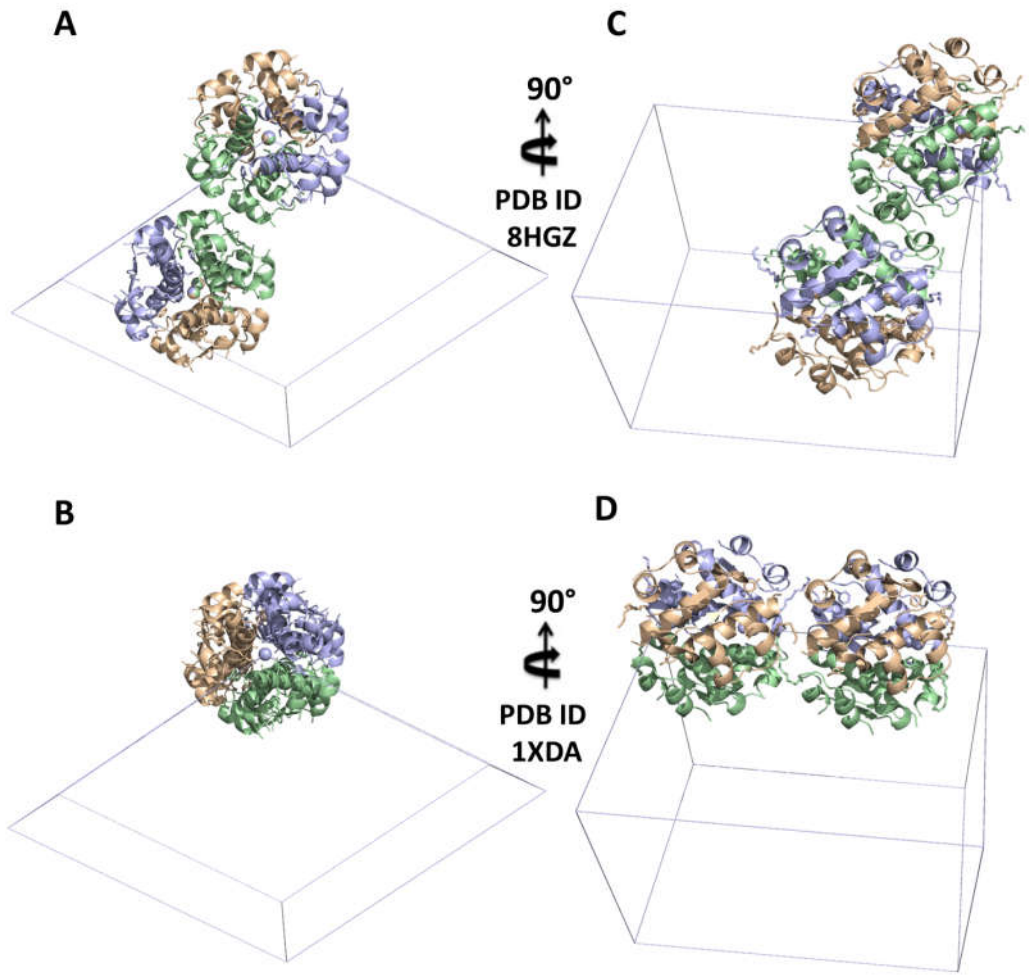

Figure 2. Comparison of the differences in unit cell origin of 8HGZ cryogenic structure and 1XDA cryogenic structure. (A) 8HGZ structure is presented in unit cell mode, also rotated 90 degrees (C). (B) 1XDA reference model is presented in unit cell mode, rotated 90 degrees (D) as well.

2.2. Comparative GNM Analysis of Detemir in Two Different Crystal Forms

The GNM analysis is a minimalist coarse-grained method to reveal a protein's dynamics [24]. Understanding the equilibrium fluctuations of the proteins is experimentally enabled by measuring the Debye-Waller/B-factor of each atom with X-ray crystallography [25,26]. Expected residue fluctuations can be obtained by GNM in favorable agreement with experimentally measured fluctuations [24]. Thus, the relation between expected residue fluctuations obtained from GNM and thermal fluctuations/B-factors can be inspected in detail [25,26]. The fluctuation profile and the orientational

 doi:10.20944/preprints202211.0412.v1

cross-correlations between pairs of nodes can also be obtained in agreement with experimental or adjustable parameters [24,25,26].

To observe if there is any difference that originated from unit cell differentiation, comparing their dynamics thoroughly, 1XDA and 8HGZ structures have been analyzed by GNM (Figure 3; Figure 4). Orientational cross-correlations between residue motions have been inspected and flexibility of the residues has been analyzed to describe the mean squared fluctuations. To investigate the communication in the residue networks, a cross-correlation map has been performed. In the cross-correlation heat-maps, blue-colored regions represent the uncorrelated motions, whereas red-colored regions represent the collective residue motions. Accordingly, chains A & B and chains C & D, chains E & F, and chains G & H have been observed as dimers with highly correlated motions in 1XDA structure (Figure 3A). In stark contrast, dimeric positive correlation in the 8HGZ detemir structure cannot be observed thoroughly due to extroverted monomers packing in the asymmetric unit cell (Figure 4A). Accordingly, the 1st dimer of the 8HGZ structure (chain A&B and chain E&F) has a weak correlation within each other (Figure 4A, bottom), while the 2nd dimer of the 8HGZ structure (chain C&D and chain G&H) shows higher correlated motions compared to the first dimer (Figure S7A). In the 8HGZ crystal structure, residues 11, 33, 36, and 66-67 had ~25% correlation with residues 137, 136, 133, and 112-113 (Figure 4A bottom; Figure 4B). However, the interchain residue cross-correlation map of the 1XDA structure indicated that residue 120 had ~25% correlation with residues 54-58 and residues 68-72, while residue 70 had ~25% correlation with residues 104-108 and residues 118-122 (Figure 3A bottom; Figure 3B).

Preprints (www.preprints.org) | NOT PEER-REVIEWED | Posted: 22 November 2022 doi:10.20944/preprints202211.0412.v1

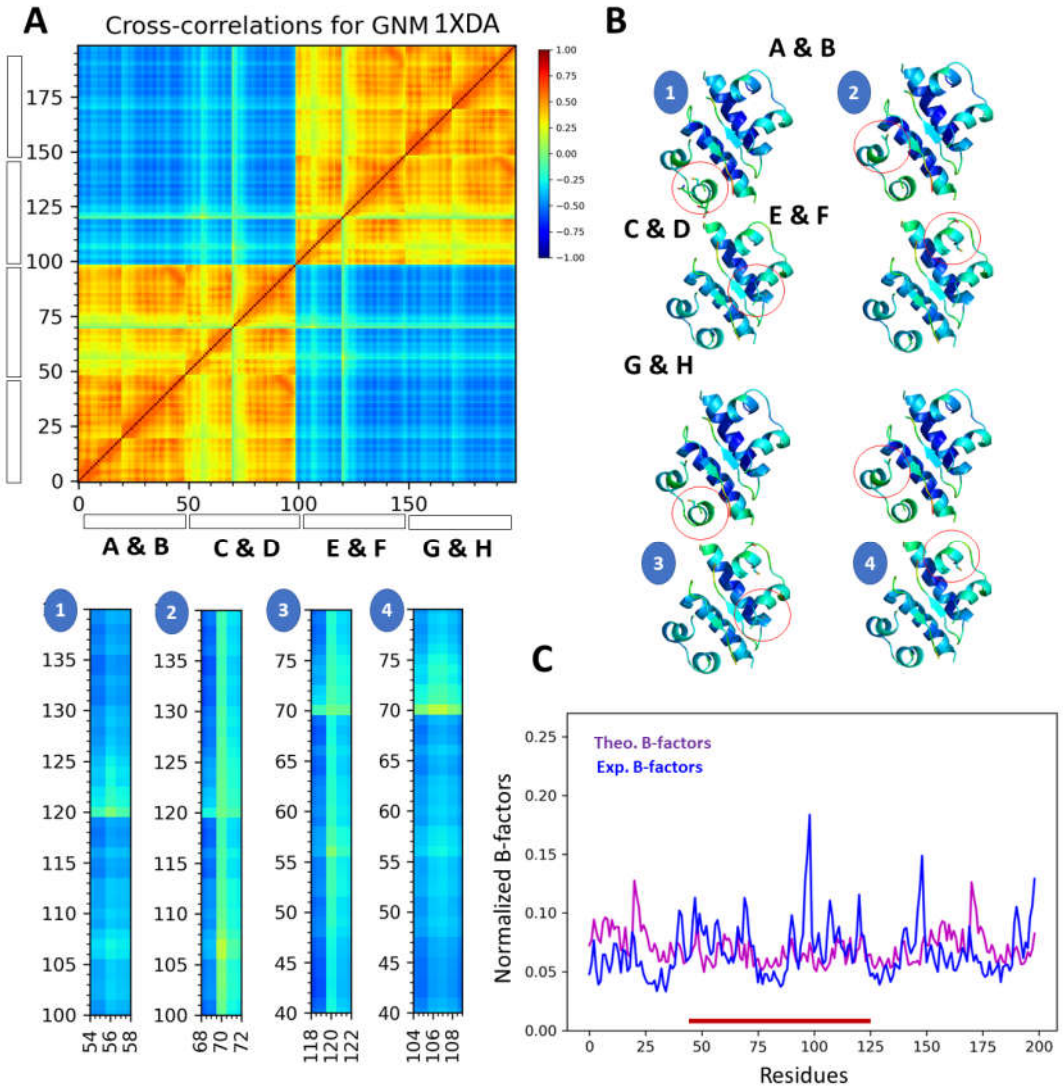

Figure 3. Gaussian Network Model (GNM) analysis results for 1XDA structure. (A) Cross-correlation heat-map from overall GNM modes for 1XDA insulin structure and ~25% correlated critical residues (54-58, 68-72, 104-108, 118-122, and 56, 70, 105-107,120) The residue pairs that move in the same direction is colored in red regions (C_{ij}orient > 0); the residue pairs moving in opposite directions are colored in blue regions (C_{ij}orient < 0); uncorrelated pairs are colored in green (C_{ij}orient = 0.0; color-code bar on the right scale). (B) Cartoon representation of 1XDA structure colored in B-factor. Critical residues corresponding to the heat map are numbered and emphasized in red circles. (C) Normalized B-factors of 1XDA are colored in blue, and theoretical B-factors calculated by GNM are colored in magenta. Critical residues corresponding to the heat map are emphasized in the red line.

On the other hand, the chain A & B displays at least 75% intramolecular correlation, followed by chain G & H, which indicates higher (at least 50%) intramolecular correlation compared to chain C & D (~50%) and chain E & F (50%) (Figure 4A). A distinct correlation has been observed at the selected cut-off distance of 8Å; in the GNM of 1XDA structure, overall correlation with B-factors was 0.650 (Figure 3C), and 0.348 in the GNM of 1XDA structure (Figure 4C). Accordingly, contrary to the theoretical B-factor calculation, the experimental B-factor calculation is characterized by the highest fluctuation around 50th, 100th, 150th, and 200th residues in 8HGZ crystal structure (Figure 4C).

Preprints (www.preprints.org) | NOT PEER-REVIEWED | Posted: 22 November 2022 doi:10.20944/preprints202211.0412.v1

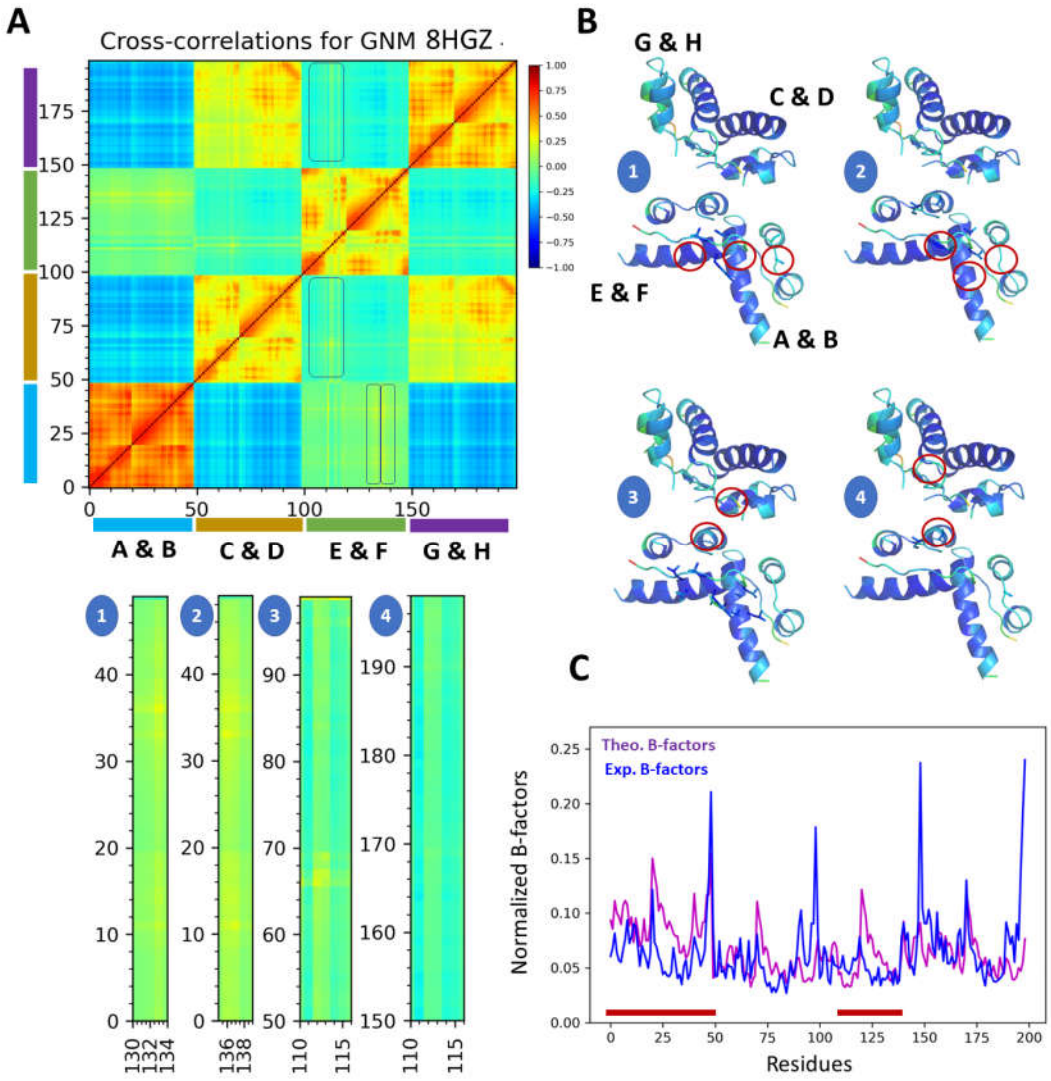

Figure 4. Gaussian Network Model (GNM) analysis results for 8HGZ structure. (A) Cross-correlation heat-map from overall GNM modes for our structure and ~25% correlated critical residues (110-115, 130-134, 136-138, and 11, 33, 36, 66-69) in chain A & B and chain E & F of the 1st dimer. The residue pairs that move in the same direction are colored in red regions (C_{ij}orient > 0); the residue pairs moving in opposite directions are colored in blue regions (C_{ij}orient < 0); uncorrelated pairs are colored in green (C_{ij}orient = 0.0; color-code bar on the right scale). (B) Cartoon representation of our structure colored in B-factor. Critical residues corresponding to the heat map are numbered and emphasized in red circles. (C) Normalized B-factors of the structure are colored in blue, and theoretical B-factors calculated by GNM are colored in magenta. Critical residues corresponding to the heat map are emphasized in red lines.

However, the B-factor analysis of the 1XDA structure around the 100th residue demonstrates higher fluctuation than other regions (Figure 3C). Remarkably, 181-182 and 190-198 regions in chain H are highly correlated with residues 68-69 in chain C (Figure S7A, B), and residues 81-82 and 90-98 in chain D (Figure S7C, D). Accordingly, when comparing the intra- and intermonomer residue motions of the 8HGZ structure, chain A & B displays at least 75% intramolecular correlation, the highest correlated chain among the others (Figure S8A, B). Interestingly, the C-terminal residues between 49-50 in chain B are highly correlated with the critical residues 73, 76-77, 81-82, 85, and 92-98 in chain D (Figure S8C, D). Similarly, the C-terminal residues 99 and 100 in chain D are highly correlated with around critical residues 123, 126-127, 130-131, 134, and 145-148 in chain F (Figure S9A, B). Likewise, the C-terminal residues 149 and 150 in chain F are highly correlated with the critical residues 173, 176-177, 180-181, 184-185, 187-188, and 195-198 in

 doi:10.20944/preprints202211.0412.v1

chain H (Figure S9C, D). Collectively, the intramonomer' correlation pattern is quite similar in each chain (Figure S8; Figure S9).

2.3. Radiation damage comparison of the 8HGZ structure and 1XDA structure

Radiation damage of two structures was calculated using the RABDAM program [27]. B Damage values were performed using the total atomic isotropic B-factor values of determined atoms. The results are presented in kernel density plots in Figure S10. The highest B Damage value of 2.05 was observed on the Asn 18 C atom (541) in chain C of the 1XDA structure, while in the 8HGZ structure, the highest B Damage value (3.11) was observed on the Glu 154 O atom (1312) (Figure S10).

3. Discussion and conclusion

Insulin detemir is the first protein structure determined with an engineered fatty acid linkage/conjugation [11]. Even though lipid modification of the proteins occurs routinely in nature, engineering strategies assist in understanding novel possibilities in oligomeric interactions, providing an enabling biotechnological tool for practical applications in drug therapy [11]. While numerous insulin structures are studied in dimer form, the presence of the fatty acid chain in the insulin paves the way to inspect the insulin in two-dimer form [7,9,10]. This provides the understanding of the dynamic profile of the molecule from an oligomeric perspective. Thus, the assembly of subunits interacting through the covalent and noncovalent bonds defines their structure-function correlations [28]. Ideally, phenolic ligands and zinc atoms retain the hexameric form of insulin [29]. The rationale for the long-acting form of the insulin detemir is characterized by keeping the molecule in the dimer form of hexamers compared to other protracted insulins [29]. Thus, after injection of the detemir subcutaneously, phenolic ligands and fatty acid groups attached to insulin rapidly diffuse into the subcutaneous area, establishing the hexamer:di-hexamer equilibrium [29]. The accumulated forms slowly dissociate into dimers and monomers, after which the myristic acid groups on insulin permit self-assembly, prolonging its action [11, 29] (Figure S2).

The oligomeric state of insulin detemir may further contribute to the understanding of monomeric-dimeric correlated motion by demonstrating comparable properties to 1XDA structure. In this work, we examined the interaction and correlation of each monomer and dimer state of the oligomeric insulin detemir whose crystal structure determined in a novel crystal packing form (Figure 1; Figure S3; Figure S4; Table 1). Notice that the presented structure here has a distinct unit cell origin compared to the 1XDA structure (Figure 2). In our structure, the first dimer has been entirely different from the second dimer (Figure 4B) and also both dimers of the 1XDA structure (Figure 3B). The two dimers of the 1XDA indicate that each dimer has an introverted state (Figure 3B), while the 8HGZ have an extroverted form in the unit cell (Figure 4B). The superposition of the first dimer of the 8HGZ with its second dimer and the two dimers of 1XDA failed due to distinct crystal packing forms (Figure S6A, B, C), while the superposition of the second dimer of the 8HGZ with two dimers of 1XDA could be achieved (Figure S6D).

In GNM analysis, the second dimer of the presented structure has a higher correlation with each other compared to its first dimer (Figure S7; Figure 4). Moreover, the C-terminal residues, Pro and Lys, in chains B, D, F, and H displayed correlated motions with the critical regions in chains D, F, and H, respectively (Figure 5; Figure S8; Figure S9).

Preprints (www.preprints.org) | NOT PEER-REVIEWED | Posted: 22 November 2022 doi:10.20944/preprints202211.0412.v1

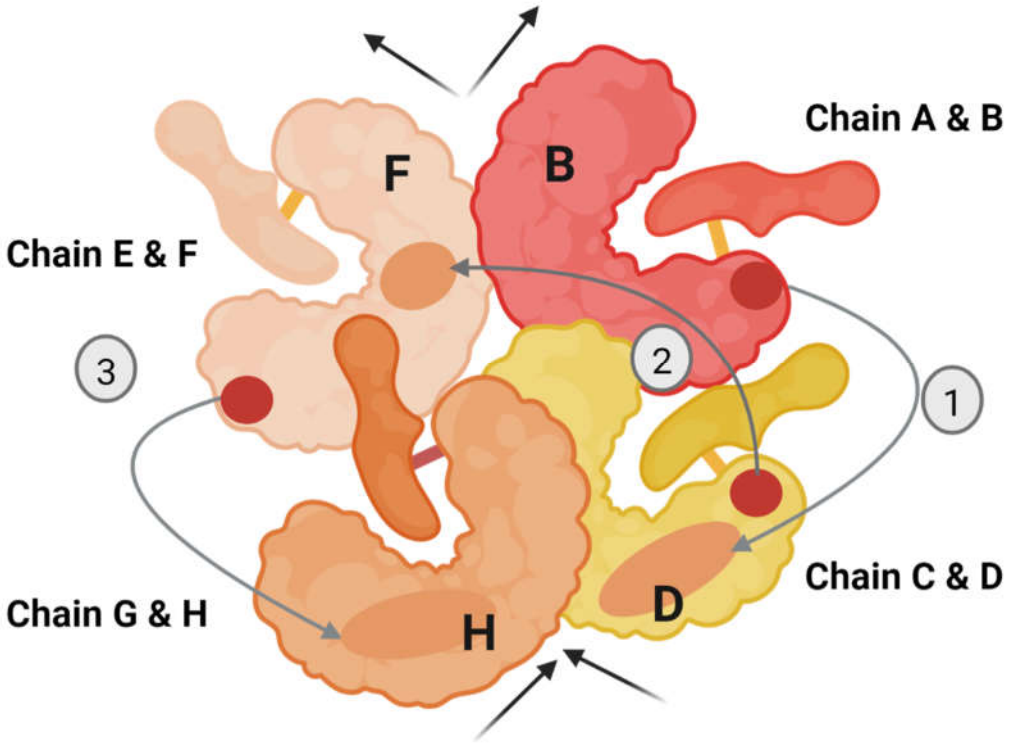

Figure 5. Pictorial representation of monomeric-dimeric correlation of the 8HGZ cryogenic structure. According to cross-correlation with GNM analysis of 8HGZ structure, the C-terminal Pro and Lys residues of chain B are highly correlated with chain D (1); the C-terminal Pro and Lys residues of chain D are highly correlated with chain F (2), and the C-terminal Pro and Lys residues of chain F are correlated with chain H (3). 8HGZ structure composed of two dimers or four monomers; compared to 1XDA structure, chain A&B and chain E&F (1st dimer) are extroverted forms (extroverted arrows) whereas chain C&D and chain G&H (2nd dimer) are slightly introverted forms (introverted arrows) than 1st dimer. Based on the intrachain' correlation, chain A&B has at least a 75% correlation with each other (colored in red); chain C&D and chain E&F correlate in intrachain up to 50% (colored in yellow, and wheat); chain G&H has at least 50% correlation with each other (colored in orange).

Interestingly, the first monomer of insulin shows at least 75% intramonomer correlation with almost all residues, followed by the last monomer of the insulin, which shows higher intramolecular correlation compared to the other chains (Figure 4A). At neutral pH, detemir exists as a dimer of dimer form [11]. The best-estimated dissociation rate of an insulin dimer into two monomers in water is 0.4 μs-1 [30]. Our best crystallization condition of the insulin detemir has occurred at pH 9. Considering that the dissociation of insulin occurs more effective at higher pH values (pH ≥ 8) and reaches the maximum by pH 10 [31], the distinct conformational arrangement of the presented structure might be closely related to the slow dissociation of the detemir' first dimer during crystallization. Correlated motion of each subunit represented in Figure 5 may confirm the causal interrelationship of the oligomeric insulin' dissociation (Figure S8; Figure S9). Additionally, observing increased fluctuations in relevant Pro and Lys residues in normalized B-factors (Figure 4C) might confirm the cooperative motion originated from the alternative conformation of the oligomeric insulin (Figure 5). Ideally, insulin lispro has been introduced as a rapid-acting insulin analog, reversing the proline at position B28 and lysine at position B29 [32]. This substitution causes a conformational shift in the C-terminal of the chain, inhibiting the ability of the insulin monomers to form dimers sterically [32]. Therefore, the dissociation constant of the dimer is reduced by 300-fold compared to regular insulin [32]. Previous studies suggest that proline has an inhibitory effect on the protein fibrillation process, promoting the retention of protein conformation [33,34]. Considering the cross-correlation of C-terminal residues with

 doi:10.20944/preprints202211.0412.v1

neighboring monomers (Figure S8; Figure S9), it could be argued that the detemir insulin demonstrates oligomeric cooperativity via the Pro and Lys residues (Pro 49, Lys 50; Pro 99, Lys 100; Pro 149, Lys 150). On the other hand, C-terminal lysine provides a platform for covalent binding of the structure with the fatty acid, allowing for the long-acting profile of the insulin [11]. Together with the GNM results, these could mean that the dissociation of the oligomeric insulin begins with the Brownian motions and fluctuations of the myristic acid.

To determine and validate the accuracy of the monomeric-dimeric correlated motion of the protracted insulins, coarse-grained normal mode analysis offers a robust dynamic profile for future studies. Considering the radiation damage of the 8HGZ structture compared to the 1XDA structure even (Figure S10), the next step is to understand the details of this dynamic profile by a time-resolved ambient temperature radiation-damage-free Serial Femtosecond X-ray (SFX) crystallographic studies supplemented with diffuse X-ray scattering.

4. Materials and Methods

4.1. Sample preparation and crystallization

The detemir sold as brand name Levemir® was crystallized by employing sitting-drop microbatch vapor diffusion screening technique under oil using 72-well Terasaki crystallization plates as explained in Ertem et al. 2022 [18]. Briefly, the detemir solution was mixed with (1:1 ratio, v/v) ~3500 commercially available sparse matrix crystallization screening conditions at ambient temperature for crystallization. Each well containing 0.83 µl protein and crystallization condition was sealed with 16.6 µL of paraffin oil (Cat#ZS.100510.5000, ZAG Kimya, Türkiye) and stored at room temperature until crystal harvesting. Terasaki plates were checked under a compound light microscope for crystal formation and growth. Large crystals were obtained within 48 hours. The best crystals were grown in a buffer containing 0.2 M sodium acetate trihydrate, 0.1 M TRIS hydrochloride pH 9.0.

4.2. Crystal harvesting

The crystals were harvested from the Terasaki crystallization plates using MiTeGen and micro loop sample pins mounted to a magnetic wand under the compound light microscope. The harvested crystals were immediately flash-frozen by plunging in the liquid nitrogen and placed in a previously cryo-cooled sample puck (Cat#M-CP-111-021, MiTeGen, USA). The filled puck within the liquid nitrogen was transferred to the dewar of the Turkish DeLight for diffraction data collection [17].

4.3. Data collection and processing

Diffraction data was collected by using Rigaku's XtaLAB Synergy Flow XRD equipped with CrysAlisPro software (Agilent, 2014) as described in Atalay et al. 2022 [17]. Before the data collection, the system was cooled to 100 K by adjusting Oxford Cryosystems's Cryostream 800 Plus. After that, the dewar was filled with liquid nitrogen and a loaded sample puck was placed into the cryo sample storage dewar installed at the Turkish DeLight. The robotic auto sample changer (UR3) mounted the MiTeGen sample pin inside the sample storage dewar to the Intelligent Goniometer Head (IGH) by the 6-axis robotic arm. The crystal was centered using the automatic centering feature of the CrysAlisPro software to the X-ray interaction position. For the data collection, the PhotonJet-R X-ray generator with Cu X-ray source was operated at full-power of 40 kV and 30 mA, and the beam intensity was set to 10% by using piezo slit system to minimize the cross-fire and overlap of the Bragg's reflections. The diffraction data, which contains 1800 frames in total, is collected to 1.7 Å resolution at a 45 mm detector distance, 0.2-degree scan width, and 1-second exposure time. The data was processed by the automatic data reduction feature of CrysAlisPro. When data reduction is completed, the output files, which contain both unmerged and unscaled files (*.rrpprof format) converted to the

 doi:10.20944/preprints202211.0412.v1

structure factor file (*.mtz format) through the *.hkl file. This step is performed by integrating CCP4 crystallography suite [19] into CrysAlisPro software.

4.4. Structure determination and refinement

The high-resolution crystal structure of detemir is determined to 1.7 Å resolution at cryogenic temperature in space group R3:H. Molecular replacement is performed by using the automated molecular replacement program PHASER [20] implemented in PHENIX software package [21] by using the previous detemir X-ray crystal structure at cryogenic temperature as a search model [11] (PDB ID: 1XDA). Coordinates of the 1XDA were used for the initial rigid-body refinement with the PHENIX software package. After simulated-annealing refinement, individual coordinates and Translation/Libration/Screw (TLS) parameters were refined. The potential positions of altered side chains and water molecules were checked in COOT [22], and positions with strong difference densities were retained. Missing water molecules were manually added, or water molecules located outside of significant electron density were removed. The Ramachandran statistics for detemir structure (most favored / additionally allowed/disallowed) are 100% / 0.0% / 0.0%, respectively. The structure refinement statistics are summarized in Table 1. All X-ray crystal structure figures were generated with PyMOL [23].

4.5. GNM analysis

The 1XDA and 8HGZ structures were analyzed by Normal Mode Analysis using ProDy [24]. Orientational cross-correlation map was defined with all Cα atoms of the proteins (residues 0-200). Myristic acids, phenols, zinc, and chloride atoms were excluded from the analysis. The cutoff distance of 8 Å was preferred in both structures to assume pairwise interactions, and the default spring constant was defined as 1.0 for both models. 1883 and 1673 atoms were parsed, and 198 non-zero modes were calculated with GNM for 8HGZ and 1XDA structures, respectively. The experimental B-factors were compared with the theoretical fluctuations calculated as well as orientational cross-correlations between residue fluctuations were calculated over all GNM modes. The differences in cross-correlations between 8HGZ and 1XDA structures were calculated at determined sections. Accordingly, intra-chain cross-correlations of each monomer in 8HGZ were compared to the intra-chain cross-correlations of each chain in the 1XDA reference model; and the interchain cross-correlations between all chains were calculated similarly, presenting as heat-maps.

Supplementary Materials: Figure S1. Alignment of detemir structure at cryogenic temperature with insulin analogs; Figure S2: Summary of the action mechanism of the insulin detemir; Figure S3. Ellipsoid and electrostatic representation of 8HGZ structure at cryogenic temperature; Figure S4. Covalent bond representation between myristic acid (MYR) and detemir; Figure S5. Superimposed two detemir structures in unit cell mode; Figure S6. A significant conformational change observed between 1XDA and 8HGZ structures in modevectors mode; Figure S7. Gaussian Network Model (GNM) analysis results for the 2nd dimer of the 8HGZ structure; Figure S8. Gaussian Network Model (GNM) analysis results for intra- and intercorrelation motion in chain A&B and chain C&D; Figure S9. Gaussian Network Model (GNM) analysis results for intra- and intercorrelation motion in chain C&D, chain E&F, and chain G&H; Figure S10. Radiation damage values were calculated using RABDAM software.

Author Contributions: Conceptualization, E.A. and H.D.; methodology, E.A. and H.D.; software, E.A., A.K., and H.D.; validation, E.A., E.D., A.K., and H.D.; formal analysis, E.A., and H.D..; investigation, E.A.; resources, E.A. and H.D.; data curation, E.A. and H.D.; writing—original draft preparation, E.A.; writing—review and editing, E.A, E.D., A.K., H.C., Ah.K., and H.D; visualization, E.A., E.D., and A.K..; supervision, E.A. and H.D..; project administration, H.D.; funding acquisition, H.D. All authors have read and agreed to the published version of the manuscript.

Funding: This research was funded by TUBITAK 2244 Industry Academia Partnership Research Project Funding Program; however, the entire responsibility of the publication belongs to the authors of the publication. The financial support received from TÜBİTAK does not mean that the content of the publication is approved in a scientific sense by TÜBİTAK.

Institutional Review Board Statement: Not applicable.

Informed Consent Statement: Not applicable.

Data Availability Statement: Coordinates of the detemir structure have been deposited in the Protein Data Bank under accession code 8HGZ.

Acknowledgments: Authors would like to dedicate this manuscript to the memory of Dr. Albert E. Dahlberg and Dr. Nizar Turker. The authors gratefully acknowledge the use of the services and facilities of the Koç University Isbank Infectious Disease Center (KUISCID). H.D. acknowledges support from NSF Science and Technology Center grant NSF-1231306 (Biology with X-ray Lasers, BioXFEL). A.K. acknowledges support from the Scientific and Technological Research Council of Türkiye (TÜBİTAK, 2218 - National Postdoctoral Research Fellowship Program under project number 118C476 and 122F301). This publication has been produced benefiting from the 2232 International Fellowship for Outstanding Researchers Program, the 1001 Scientific and Technological Research Projects Funding Program of the, 2244 Industry Academia Partnership Researcch Project Funding Program and 2236 CoCirculation2 Program of TÜBİTAK (Project Nos. 118C270, 120Z520, 119C132 and 121C063).

Conflicts of Interest: The authors declare no conflict of interest.

References

1. Home PD. Plasma insulin profiles after subcutaneous injection: How close can we get to physiology in people with diabetes? Diabetes, Obes. Metab. 2015.
2. Ismail-Beigi F, Moghissi E, Tiktin M, Hirsch B, Inzucchi SE, Genuth S. Individualizing glycemic targets in type 2 diabetes mellitus: Implications of recent clinical trials. Ann Intern Med. 2011;
3. Donner T, Sarkar S. Insulin – Pharmacology, Therapeutic Regimens And Principles Of Intensive Insulin Therapy. Endotext. 2019.
4. Tisch R, McDevitt H. Insulin-dependent diabetes mellitus. Cell [Internet]. Elsevier B.V.; 1996 [cited 2022 Nov 16];85:291–7. Available from: http://www.cell.com/article/S009286740081106X/fulltext
5. Owens DR, Zinman B, Bolli GB. Insulins today and beyond. Lancet. 2001.
6. Pillai O, Panchagnula R. Insulin therapies - Past, present and future. Drug Discov. Today. 2001.
7. Ayan E, DeMirci H. A Brief Atlas of Insulin. Curr Diabetes Rev [Internet]. Curr Diabetes Rev; 2022 [cited 2022 Nov 16];19. Available from: https://pubmed.ncbi.nlm.nih.gov/35692127/
8. Freeman JS. Insulin analog therapy: Improving the match with physiologic insulin secretion. J. Am. Osteopath. Assoc. 2009.
9. Vajo Z, Duckworth WC. Genetically engineered insulin analogs: Diabetes in the new millenium. Pharmacol. Rev. 2000.
10. Rosskamp RH, Park G. Long-acting insulin analogs. Diabetes Care. 1999.
11. Whittingham JL, Havelund S, Jonassen I. Crystal structure of a prolonged-acting insulin with albumin-binding properties. Biochemistry. 1997;
12. Hamdan II, Farah DGH, Khalil EA, Mansour RSH, Abdel-Halim H. Interaction of esomeprazole with insulin detemir and human albumin: A potential cause of hypoglycemia. Biophys Chem. Elsevier; 2022;285:106809.
13. Kaplan W, Afandi B, Hassani N Al. Comparison between Insulin Glargine and Insulin Detemir in Adolescents with Type 1 Diabetes during Ramadan Fasting. J Diabetes Endocr Pract [Internet]. Thieme Medical and Scientific Publishers Pvt. Ltd.; 2022 [cited 2022 Nov 16]; Available from: http://www.thieme-connect.com/products/ejournals/html/10.1055/s-0042-1753496
14. Frier BM, Russell-Jones D, Heise T. A comparison of insulin detemir and neutral protamine hagedorn (isophane) insulin in the treatment of diabetes: A systematic review. Diabetes, Obes. Metab. 2013.
15. Setoodeh A, Rabbani A, Sayarifard F, Haghshenas Z, Sayarifard A, Rostami P, et al. Comparison of Once-daily versus Twice-daily Injection of Insulin Detemir in Children with Type 1 Diabetes Mellitus. Iran J Pediatr 2022 326 [Internet]. Brieflands; 2022 [cited 2022 Nov 16];32:116461. Available from: https://brieflands.com/articles/ijp-116461.html
16. Havelund S, Plum A, Ribel U, Jonassen I, Vølund A, Markussen J, et al. The mechanism of protraction of insulin detemir, a long-acting, acylated analog of human insulin. Pharm Res. 2004;
17. Atalay N, Akcan EK, Gül M, Ayan E, Destan E, Ertem FB, et al. Cryogenic X-ray crystallographic studies of biomacromolecules at Turkish Light Source "Turkish DeLight." bioRxiv [Internet]. Cold Spring Harbor Laboratory; 2022 [cited 2022 Nov 16];10:2022.09.03.506456. Available from: https://www.biorxiv.org/content/10.1101/2022.09.03.506456v1
18. Ertem FB, Guven O, Buyukdag C, Gocenler O, Ayan E, Yuksel B, et al. Protocol for structure determination of SARS-CoV-2 main protease at near-physiological-temperature by serial femtosecond crystallography. STAR Protoc [Internet]. STAR Protoc; 2022 [cited 2022 Mar 29];3. Available from: https://pubmed.ncbi.nlm.nih.gov/35194584/
19. Winn MD, Ballard CC, Cowtan KD, Dodson EJ, Emsley P, Evans PR, et al. Overview of the CCP4 suite and current developments. Acta Crystallogr. Sect. D Biol. Crystallogr. 2011.
20. McCoy AJ, Grosse-Kunstleve RW, Adams PD, Winn MD, Storoni LC, Read RJ. Phaser crystallographic software. J Appl Crystallogr. 2007;

 doi:10.20944/preprints202211.0412.v1

21. Adams PD, Afonine P V., Bunkóczi G, Chen VB, Davis IW, Echols N, et al. PHENIX: A comprehensive Python-based system for macromolecular structure solution. Acta Crystallogr Sect D Biol Crystallogr. 2010;
22. Emsley P, Lohkamp B, Scott WG, Cowtan K. Features and development of Coot. Acta Crystallogr Sect D Biol Crystallogr. 2010;
23. DeLano WL. The PyMOL Molecular Graphics System, Version 2.3. Schrödinger LLC. 2020.
24. Bakan A, Meireles LM, Bahar I. ProDy: Protein dynamics inferred from theory and experiments. Bioinformatics. 2011;
25. Bahar I, Wallqvist A, Covell DG, Jernigan RL. Correlation between native-state hydrogen exchange and cooperative residue fluctuations from a simple model. Biochemistry. 1998;
26. Bahar I, Atilgan AR, Demirel MC, Erman B. Vibrational dynamics of folded proteins: Significance of slow and fast motions in relation to function and stability. Phys Rev Lett. 1998;
27. Shelley KL, Dixon TPE, Brooks-Bartlett JC, Garman EF. RABDAM: quantifying specific radiation damage in individual protein crystal structures. J Appl Crystallogr. 2018;
28. Ayan E, Yuksel B, Destan E, Ertem FB, Yildirim G, Eren M, et al. Cooperative allostery and structural dynamics of streptavidin at cryogenic- and ambient-temperature. Commun Biol. 2022;
29. Poon K, King AB. Glargine and detemir: Safety and efficacy profiles of the long-acting basal insulin analogs. Drug. Healthc. Patient Saf. 2010.
30. Acharya S, Mondal S, Mukherjee S, Bagchi B. Rate of Insulin Dimer Dissociation: Interplay between Memory Effects and Higher Dimensionality. J Phys Chem B. 2021;
31. Fredericq E. Reversible dissociation of insulin [10]. Nature. 1953.
32. Holleman F. Insulin lispro (revision number 20). Diapedia. 2015.
33. Li SC, Goto NK, Williams KA, Deber CM. α-Helical, but not β-sheet, propensity of proline is determined by peptide environment. Proc Natl Acad Sci U S A. 1996;
34. Samuel D, Ganesh G, Yang P-W, Chang M-M, Wang S-L, Hwang K-C, et al. Proline inhibits aggregation during protein refolding. Protein Sci. 2008;